

# Machine-learning force-field models for dynamical simulations of metallic magnets

Gia-Wei Chern,<sup>1,\*</sup> Yunhao Fan,<sup>1</sup> Sheng Zhang,<sup>1</sup> and Puhan Zhang<sup>1</sup>

<sup>1</sup>*Department of Physics, University of Virginia, Charlottesville, VA 22904, USA*

We review recent advances in machine-learning (ML) force-field methods for Landau-Lifshitz-Gilbert (LLG) simulations of itinerant electron magnets, focusing on their scalability and transferability. Built on the principle of locality, a deep neural-network model is developed to efficiently and accurately predict electron-mediated forces governing spin dynamics. Symmetry-aware descriptors constructed through a group-theoretical approach ensure rigorous incorporation of both lattice and spin-rotation symmetries. The framework is demonstrated using the prototypical s-d exchange model widely employed in spintronics. ML-enabled large-scale simulations reveal novel nonequilibrium phenomena, including anomalous coarsening of tetrahedral spin order on the triangular lattice and the freezing of phase-separation dynamics in lightly hole-doped, strong-coupling square-lattice systems. These results establish ML force-field frameworks as scalable, accurate, and versatile tools for modeling nonequilibrium spin dynamics in itinerant magnets.

## I. INTRODUCTION

Itinerant frustrated magnets host a rich variety of spin and electronic textures stabilized by electron-mediated interactions. Among them, magnetic vortices and skyrmions have attracted particular attention for their topological stability and potential spintronic applications [1–7]. The Berry phases associated with these textures act as emergent magnetic fields, giving rise to novel transport phenomena such as the anomalous Hall effect. Another striking example is the mixed-phase state in colossal magnetoresistance (CMR) manganites, where ferromagnetic metallic and antiferromagnetic or charge-ordered insulating regions coexist [8–16]. These nanoscale textures are highly responsive to external stimuli—magnetic fields, pressure, or doping—leading to dramatic transport changes.

Modeling the real-time dynamics of such complex spin textures remains computationally challenging. While classical spins evolve according to the Landau-Lifshitz-Gilbert (LLG) equation, the effective fields driving the dynamics originate from quantum electron–spin exchange interactions. Direct simulations are therefore prohibitively expensive, as each LLG step requires solving a many-body electronic problem. Machine learning (ML) offers a powerful alternative. As emphasized by Kohn [17, 18], linear-scaling electronic algorithms hinge on the principle of locality—a concept naturally realized in Behler-Parrinello (BP)-type ML force-field frameworks developed for *ab initio* molecular dynamics [19–33] and extended to adiabatic lattice dynamics in condensed-matter systems [34–37].

Here, we present a scalable ML force-field framework for the adiabatic dynamics of itinerant magnets, generalizing the BP architecture [38–42]. A central feature is the use of symmetry-preserving magnetic descriptors that remain invariant under lattice point-group and spin-rotation operations while being differentiable with re-

spect to spin orientations. We demonstrate the method for the one-band s-d exchange model, widely used in spintronics. ML-trained force fields reproduce noncoplanar tetrahedral spin order and its anomalous coarsening dynamics on the triangular lattice [42], and reveal a correlation-induced freezing phenomenon in the phase-separated state of a lightly hole-doped, strong-coupling square-lattice system [38].

## II. BEHLER-PARRINELLO FORCE-FIELD ARCHITECTURE

We consider a one-band s-d model, as a representative system for itinerant magnets, described by the following Hamiltonian

$$\hat{\mathcal{H}} = - \sum_{ij,\alpha} t_{ij} \left( \hat{c}_{i\alpha}^\dagger \hat{c}_{j\alpha} + \text{h.c.} \right) - J \sum_{i,\alpha\beta} \mathbf{S}_i \cdot \hat{c}_{i\alpha}^\dagger \boldsymbol{\sigma}_{\alpha\beta} \hat{c}_{i\beta}. \quad (1)$$

Here  $\hat{c}_{i\alpha}^\dagger$  ( $\hat{c}_{i\alpha}$ ) is the creation (annihilation) operators of an electron with spin  $\alpha = \uparrow, \downarrow$  at site- $i$ . The first term describes the Hamiltonian for the  $s$ -electrons, while  $J$  in the second term represents the exchange coupling between local magnetic moment  $\mathbf{S}_i$  from the  $d$ -electrons and spin of  $s$ -electrons. Here the local moments are approximated by classical spins with a fixed unit length.

The dynamics of the classical local spins is governed by the Landau-Lifshitz-Gilbert equation

$$\frac{d\mathbf{S}_i}{dt} = \gamma \mathbf{S}_i \times (\mathbf{H}_i + \boldsymbol{\eta}_i) - \gamma \lambda \mathbf{S}_i \times [\mathbf{S}_i \times (\mathbf{H}_i + \boldsymbol{\eta}_i)]. \quad (2)$$

Here,  $\gamma$  denotes the gyromagnetic ratio,  $\lambda$  is a dimensionless damping parameter,  $\mathbf{H}_i$  is the local effective field arising from the s-d exchange interaction with itinerant electrons, and  $\boldsymbol{\eta}_i$  represents the stochastic magnetic field associated with thermal fluctuations modeled as a Gaussian random process.

Within the adiabatic approximation—analogue to the Born-Oppenheimer scheme in quantum MD [43], the local exchange force is given by the derivative of an effective

\* [gchern@virginia.edu](mailto:gchern@virginia.edu); Corresponding author

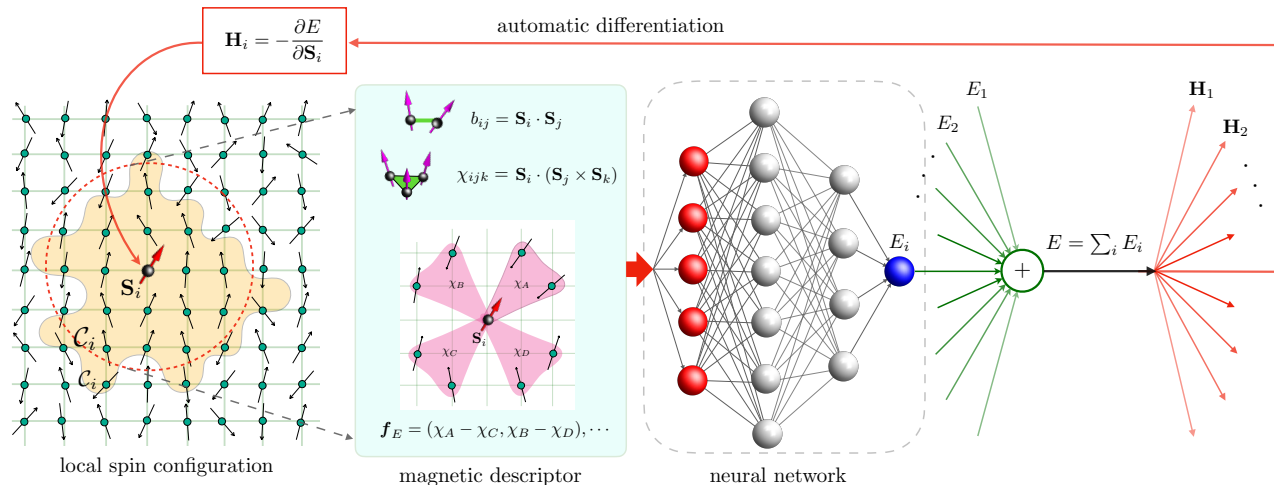


FIG. 1. Schematic diagram of ML force-field model for itinerant electron magnets. A descriptor transforms the neighborhood spin configuration  $\mathcal{C}_i$  to effective coordinates  $\{p_r^\Gamma, \eta_r^\Gamma\}$  which are then fed into a neural network (NN). The output node of the NN corresponds to the local energy  $\epsilon_i = \varepsilon(\mathcal{C}_i)$  associated with spin  $\mathbf{S}_i$ . The corresponding total potential energy  $E$  is obtained from the summation of these local energies. Automatic differentiation is employed to compute the derivatives  $\partial E / \partial \mathbf{S}_i$  from which the local exchange fields  $\mathbf{H}_i$  are obtained.

spin-dependent energy  $E = E(\{\mathbf{S}_i\})$ :

$$\mathbf{H}_i = -\frac{\partial E}{\partial \mathbf{S}_i} \quad (3)$$

Formally, this effective energy can be obtained by integrating out electrons given a frozen spin configuration. For example, in the weak-coupling limit ( $J \ll t_{ij}$ ), second-order perturbation theory yields an RKKY-type long-range spin-spin interaction [44–46]. At intermediate to strong coupling, a systematic expansion is, however, exceedingly cumbersome and often impractical. The effective energy can be computed by numerically integrating out electrons on-the-fly,

$$E = \langle \hat{\mathcal{H}}(\{\mathbf{S}_i\}) \rangle = \text{Tr}(\hat{\rho}_e \hat{\mathcal{H}}), \quad (4)$$

with  $\hat{\rho}_e = e^{-\beta \hat{\mathcal{H}}} / \mathcal{Z}$  the equilibrium density matrix for a fixed spin configuration and  $\mathcal{Z} = \text{Tr} e^{-\beta \hat{\mathcal{H}}}$  the partition function. Since the Hamiltonian is quadratic in fermionic operators, exact diagonalization (ED) can be employed, but its  $\mathcal{O}(N^3)$  scaling makes large-scale LLG simulations prohibitive. More efficient schemes, such as the linear-scaling kernel polynomial method (KPM), are available, though their implementation is intricate and they cannot treat systems with electron-electron interactions.

Machine learning (ML) methods provide a general linear-scaling approach to computing effective local fields  $\mathbf{H}_i$ . As pointed out by W. Kohn, such scaling is enabled by the locality principle, or the “nearsightedness” of many-electron systems [17, 18]. This principle implies that extensive quantities can be evaluated through a divide-and-conquer strategy. Indeed, the locality principle underlies modern ML-based force-field methods that enable large-scale MD simulations with quantum accuracy [19–32]. A linear-scaling framework exploiting this

principle was pioneered by Behler-Parrinello (BP) [19] and Bartók *et al.* [20]. Here, we extend the BP architecture to predict local exchange fields in itinerant spin systems.

A schematic of the ML force-field model is shown in Fig. 1. The effective energy  $E$ , defined in Eq. (4), is decomposed into local contribution  $\epsilon_i$  associated with lattice site- $i$ ,

$$E = \sum_i \epsilon_i = \sum_i \varepsilon(\mathcal{C}_i). \quad (5)$$

In the second expression, we invoke the locality principle, assuming that the site energy  $\epsilon_i$  depends only on the local magnetic environment, denoted as  $\mathcal{C}_i$ , through a universal function  $\varepsilon(\cdot)$  which is determined by the underlying electron Hamiltonian. In practical implementations, the neighborhood is defined as the collection of spins within a cutoff radius  $r_c$  around the  $i$ -th site:  $\mathcal{C}_i = \{\mathbf{S}_j \mid |\mathbf{r}_j - \mathbf{r}_i| < r_c\}$ . The complex functional dependence of the local energy on the magnetic environment is to be approximated by a deep-learning neural network. The effective local field  $\mathbf{H}_i$ , defined as the derivative of the total energy [Eq. (3)], can be efficiently computed using automatic differentiation [47, 48].

A key component of the ML force-field model is the representation, or descriptor, of local spin configurations  $\mathcal{C}_i$ . In BP-type schemes, the output energy  $\epsilon_i$  is a scalar and must remain invariant under the system’s symmetry operations. Thus, descriptors must both distinguish distinct spin configurations and preserve the underlying symmetries of the electron model. Descriptors play a similarly central role in BP-type force fields for quantum MD, where they are required to respect symmetry operations, such as translation, rotation, and reflection, of the 3D Euclidean group  $E(3)$ , as well as per-

mutation of identical atoms [19–21, 49–54].

Here we employ group-theoretical methods to construct magnetic descriptors for the s-d model. In contrast to atomic descriptors in MD systems, where the relevant symmetry is the full  $E(3)$  group, the lattice-based s-d model reduces this to the discrete translation group and the on-site point group [34, 55, 56]. In addition, the model possesses a continuous symmetry: the s-d Hamiltonian is invariant under global  $SO(3)/SU(2)$  spin rotations [39]. The local energy function  $\varepsilon(\mathcal{C}_i)$  must respect both spin-rotation and lattice symmetries. To this end, we first note that spin-rotation invariance is ensured by expressing  $\varepsilon(\mathcal{C}_i)$  in terms of bond variables  $b_{jk}$  and scalar chiralities  $\chi_{jmn}$ ,

$$b_{jk} = \mathbf{S}_j \cdot \mathbf{S}_k, \quad \chi_{jmn} = \mathbf{S}_j \cdot \mathbf{S}_m \times \mathbf{S}_n, \quad (6)$$

which correspond to two- and three-spin correlations.

For lattice symmetries, we first decompose the set of bond/chirality variables  $\{b_{jk}, \chi_{jmn}\}$  around site- $i$ , which forms a basis of a high-dimensional representation of the on-site point group into irreducible representations (IRs). For instance, consider the four chirality variables  $\chi_A, \chi_B, \chi_C, \chi_D$  in Fig. 1 for a square lattice with on-site symmetry group  $D_4$ . The decomposition is  $4 = A_1 + B_1 + E$ , with corresponding IR coefficients:  $f^{A_1} = \chi_A + \chi_B + \chi_C + \chi_D$ ,  $f^{B_1} = \chi_A - \chi_B + \chi_C - \chi_D$ , and  $f^E = (\chi_A - \chi_C, \chi_B - \chi_D)$ . For each fundamental IR, we collect its component coefficients into a vector  $\mathbf{f}^{(\Gamma, r)} = (f_1^{(\Gamma, r)}, \dots, f_{n_\Gamma}^{(\Gamma, r)})$ , where  $\Gamma$  denotes the IR,  $n_\Gamma$  its dimension, and  $r$  the multiplicity. A basic class of invariants is the power spectrum,

$$p_r^\Gamma = |\mathbf{f}_r^\Gamma|^2. \quad (7)$$

While the power spectrum ignores relative phases between IRs, these can be incorporated through bispectrum coefficients  $b_{r, r_1, r_2}^\Gamma$  [51, 57], constructed from triple products of IR coefficients and Clebsch-Gordon coefficients. Because IRs often have large multiplicities, bispectrum descriptors can be numerous and redundant. To reduce complexity, we introduce reference IR coefficients  $\mathbf{f}_{\text{ref}}^\Gamma$  [34, 39, 55], obtained from the IR decomposition of bond and chirality variables coarse-grained over large blocks. These define a phase variable,

$$\eta_r^\Gamma \equiv \mathbf{f}_r^\Gamma \cdot \mathbf{f}_{\text{ref}}^\Gamma / |\mathbf{f}_r^\Gamma| |\mathbf{f}_{\text{ref}}^\Gamma|, \quad (8)$$

allowing relative phases to be inferred consistently. The final feature set thus consists of amplitudes  $p_r^\Gamma$ , phases  $\eta_r^\Gamma$ , and a selected set of bispectrum coefficients obtained from the reference IR. The site energy  $\epsilon_i$ , produced by the NN, depends only on these invariants, thereby preserving the full symmetry of the s-d model.

As discussed above, one of the major advantages of the proposed scalable ML framework is its dramatically enhanced computational efficiency—both in terms of algorithmic complexity and actual runtime. For instance,

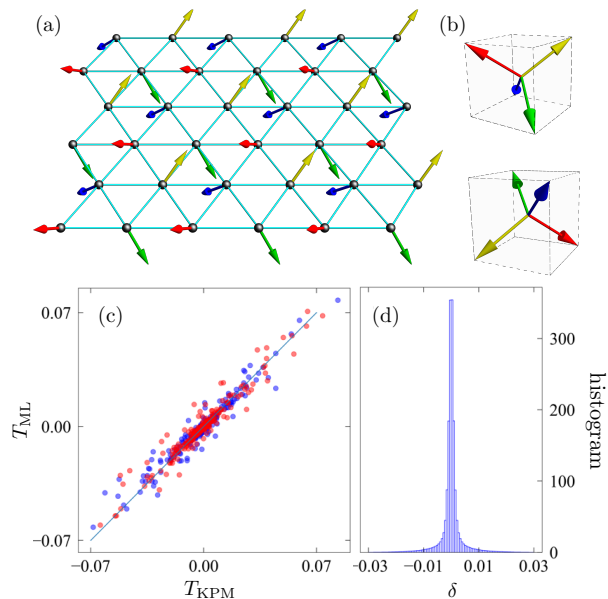


FIG. 2. (a) Tetrahedral spin order on a triangular lattice [Eq. (9)]. (b) Two inequivalent spins in a quadrupled unit cell with opposite chirality. (c) Comparison of ML-predicted torque  $T_{\text{ML}}$  with KPM results  $T_{\text{KPM}}$ , where  $\mathbf{T}_i = \mathbf{S}_i \times \mathbf{H}_i$ . (d) Histogram of prediction error  $\delta = T_{\text{KPM}} - T_{\text{ML}}$ .

a 10,000-time-step simulation of a  $50 \times 50$  system using the exact-diagonalization (ED) method requires approximately 20 CPU hours. While limited parallelization on GPU can offer a modest improvement, the ED calculation based on the LAPACK package is inherently non-parallelizable. In contrast, the same simulation performed with the ML force-field model takes only about 5 minutes, representing nearly a three-order-of-magnitude ( $\sim 1000$ -fold) speedup. This dramatic improvement stems from the difference in computational scaling— $\mathcal{O}(N^3)$  for the ED approach versus linear  $\mathcal{O}(N)$  scaling for the ML model. Even when compared with the KPM, which also exhibits linear scaling and can be efficiently implemented on GPU, the ML framework remains superior. A 500-step simulation of a  $96 \times 96$  system takes about 100 minutes using KPM, whereas the same run with the ML model requires only around 20 minutes, demonstrating an additional  $\sim 5$ -fold gain in efficiency.

### III. CHIRAL DOMAIN COARSENING OF TETRAHEDRAL SPIN ORDER

We first apply the above ML framework to the nearest-neighbor triangular-lattice s-d model at electron filling fraction  $f \sim 1/4$ . Notably, the ground state at this filling fraction as well as  $f = 3/4$  is a non-coplanar tetrahedral order with a quadrupled unit cell [58–62]. In this order, the local spins point toward the corners of a regular tetrahedron; see Fig. 2(a) and (b). More generally, magnetic orders with a quadrupled unit cell on the triangular

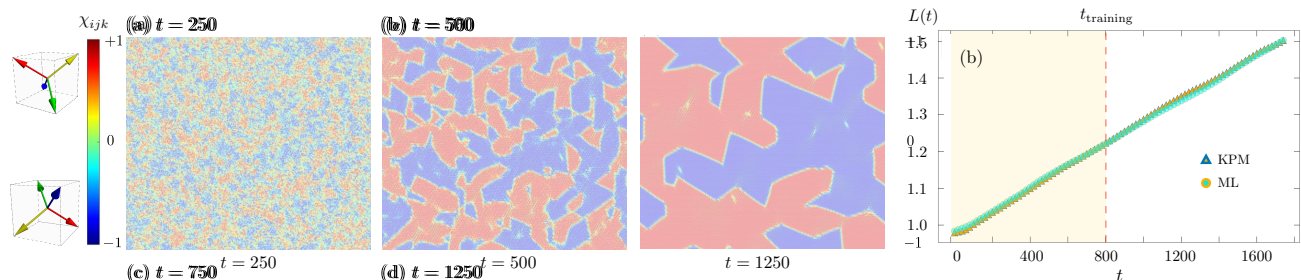


FIG. 3. (a) Snapshots of local scalar chirality  $\chi_{ijk} = \mathbf{S}_i \cdot \mathbf{S}_j \times \mathbf{S}_k$ , with  $(ijk)$  denoting sites of an elementary triangle, at different times after a thermal quench of the triangular s-d model near  $n = 1/4$ . (b) Characteristic length  $L$  versus time, extracted from the chirality structure factor (linear scales on both axes). Yellow triangles and green circles show data from LLG quenches using KPM and ML-calculated fields, respectively. The ML model was trained only on KPM-LLG data up to  $t_{\text{training}} = 800$ , marked by the yellow shaded region.

lattice can be described by a triple- $\mathbf{Q}$  structure,

$$\mathbf{S}_i = \Delta_1 e^{i\mathbf{M}_1 \cdot \mathbf{r}_i} + \Delta_2 e^{i\mathbf{M}_2 \cdot \mathbf{r}_i} + \Delta_3 e^{i\mathbf{M}_3 \cdot \mathbf{r}_i}, \quad (9)$$

with ordering vectors  $\mathbf{M}_1 = (2\pi/a, 0)$  and  $\mathbf{M}_{2,3} = (-\pi/a, \pm\sqrt{3}\pi/a)$  at the midpoints of the hexagonal Brillouin zone (BZ) edge, and vector order parameters  $\Delta_\eta$ . The symmetric tetrahedral state corresponds to  $\Delta_\eta = \Delta \hat{\mathbf{e}}_\eta$ , where  $\Delta$  is the amplitude and  $\hat{\mathbf{e}}_\eta$  ( $\eta = 1, 2, 3$ ) are three orthogonal unit vectors, yielding spins at the corners of a regular tetrahedron.

The tetrahedral order is further characterized by a discrete  $Z_2$  symmetry associated with the handedness of the spin texture. The scalar chirality on a triangular plaquette is defined as  $\chi_{ijk} = \mathbf{S}_i \cdot \mathbf{S}_j \times \mathbf{S}_k$ , which takes the uniform value  $\chi_{ijk} = \pm 4S^3/3\sqrt{3}$  in the perfect tetrahedral state. The two signs correspond to an Ising-like  $Z_2$  symmetry spontaneously broken at low temperatures. The associated electronic state exhibits striking transport and magnetoelectric properties. In particular, the chiral spin order produces a quantized Hall conductivity  $\sigma_{xy} = \pm e^2/h$  without external magnetic fields [58, 63].

Although long-range tetrahedral order is destroyed by thermal fluctuations in 2D, the  $Z_2$  chirality order survives at finite temperature. Monte Carlo simulations of the triangular s-d model at  $n \approx 1/4$  [60] revealed a chiral phase transition that, despite its Ising-like order parameter, is strongly first order. This deviation from the expected 2D Ising universality suggests that the coarsening dynamics of chiral domains may also differ from the Allen-Cahn growth law expected for 2D Ising model. To investigate this, we built a ML force field model for the triangular-lattice s-d model with Hund's rule coupling  $J = 3$ , and a chemical potential  $\mu = -3.2$ , corresponding to a filling fraction  $n \approx 1/4$ ; here both energies are measured in units of the nearest-neighbor hopping  $t_{\text{nn}}$ . The training dataset were obtained from KPM method [64–66].

The neural network was implemented in PyTorch [67] and consists of eight hidden layers with  $2048 \times 1024 \times 512 \times 256 \times 128 \times 64 \times 64 \times 64$  neurons. The input layer contains 1806 nodes, corresponding to the feature variables  $G_r^T$ , while the single output neuron predicts the local energy. Rectified Linear Unit (ReLU) activations [68] are used between layers, and the network

is optimized using the Adam algorithm [69]. Since the torque  $\mathbf{T}_i = \mathbf{S}_i \times \mathbf{H}_i$  is the primary driving force in LLG spin dynamics, the loss function incorporates the mean-square errors (MSE) of both the local torques and total energy:  $L = \sum_{i=1}^N \left| \mathbf{T}_i - \hat{\mathbf{T}}_i \right|^2 + \eta_E \left| E - \sum_{i=1}^N \hat{e}_i \right|^2$ , where quantities with hats denote ML predictions and  $\eta_E$  controls the relative weight of the energy term. Two models were trained: one using only the torque loss ( $\eta_E = 0$ ) and another with  $\eta_E = 0.01$ . The benchmark of the  $\eta_E = 0$  model is shown in Fig. 2(c,d), the predicted forces agree well with the exact results, achieving an MSE of  $1.64 \times 10^{-5}$  per spin without signs of overfitting. Additional dynamical benchmarks are provided in Ref. [42]. We also note that although both achieve similar MSE values, including the energy term generally makes training more difficult. Since LLG simulations depend directly on the predicted torques, it is practical to begin training with the torque-only loss and gradually introduce the energy term by increasing  $\eta_E$  in later epochs. The training of the the above NN models with 8 hidden layers took about  $\sim 5$  days to reach the reported MSE.

Next we applied the trained ML model to perform large-scale thermal quench simulations of the s-d model. An initial state with random spins was suddenly coupled to a thermal bath at low temperature  $T = 0.01$ . Fig. 3(a) shows snapshots of the local scalar chirality  $\chi_\Delta(\mathbf{r})$  at successive times following a thermal quench at  $t = 0$ , with color indicating the chirality magnitude. Initially, the random spin configuration produces a disordered chirality pattern. As relaxation proceeds, domains of uniform chirality emerge and grow. These domains are separated by sharp interfaces, only a few lattice constants wide, across which the chirality vanishes.

The characteristic size  $L(t)$  of chiral domains is obtained from the inverse width  $\Delta q^{-1}$  of the  $\mathbf{q} = 0$  peak in the ensemble-averaged chirality structure factor. Fig. 3(b) compares  $L(t)$  from LLG simulations using ML- and KPM-calculated fields, showing excellent agreement and confirming that the ML force field accurately reproduces the phase-ordering dynamics. Notably, although the ML model was trained only on KPM-LLG data up to  $t_{\text{training}} = 800$ , it continues to predict  $L(t)$  reliably at

much longer times, demonstrating strong extrapolation beyond the training window.

More importantly, we find that the chiral domain size grows linearly with time,  $L(t) \sim L_0 + a(t - t_0)$ , in sharp contrast to the Allen–Cahn law  $L \sim \sqrt{t}$  expected for a non-conserved Ising order parameter. Since the Allen–Cahn behavior arises from curvature-driven domain motion, the observed linear growth likely reflects the distinctive domain morphology. As shown in Fig. 3(a), late-stage chiral domains exhibit nearly straight interfaces aligned with the principal symmetry directions of the triangular lattice. The zero curvature of these straight boundaries implies vanishing domain-wall motion under the Allen–Cahn mechanism. In this case, domain growth is most likely governed by the dynamics of sharp corners, suggesting the need for a theoretical framework of chiral-domain coarsening based on corner motion as point defects.

#### IV. PHASE SEPARATION DYNAMICS OF DOUBLE-EXCHANGE MODELS

In this section, we apply the ML force-field framework to study phase-separation dynamics in the strong-coupling, or double-exchange [70–72], regime of the  $s$ - $d$  model. Phase separation phenomena play a central role in the behavior and functionality of many strongly correlated electron systems [8–13, 73–76]. A prominent example is the complex inhomogeneous states observed in manganites and magnetic semiconductors exhibiting the colossal magnetoresistance (CMR) effect [8–13]. These nanoscale textures arise from the segregation of hole-rich ferromagnetic clusters within half-filled antiferromagnetic domains [14–16]. Because the number of doped carriers is conserved, the segregation dynamics follow the classic theory of Lifshitz, Slyozov, and Wagner (LSW) [77, 78], which predicts a coarsening exponent  $\alpha = 1/3$ .

The square-lattice double-exchange model has been extensively studied theoretically [79–83]. In the regime of slight hole doping from half-filling, a mixed-phase state – consisting of hole-rich ferromagnetic puddles embedded in a half-filled antiferromagnetic insulator – emerges as a stable thermodynamic phase at strong Hund’s coupling [80–82]. Despite extensive research on the static properties of such mixed-phase states in CMR materials, the kinetics of electron-correlation-driven phase separation remain largely unexplored. Fundamental questions, such as whether the process exhibits dynamical scaling and whether late-stage domain growth follows the LSW power law, are still open. The superior scalability of the ML force-field framework provides a powerful means to address these questions through large-scale simulations of phase separation in this model.

We trained a six-layer neural network (NN) using PyTorch [67, 68] on 3500 snapshots of spin configurations and local exchange forces from ED–LLG simulations on

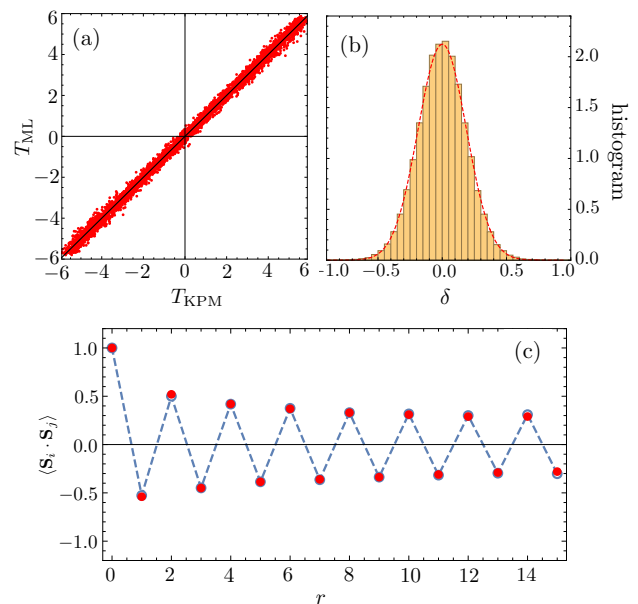


FIG. 4. (a) ML-predicted exchange fields versus exact results from the test dataset. (b) The distribution of the force difference  $\delta = H_{\text{ML}} - H_{\text{exact}}$ , well fitted by a normal distribution (red line) with variance  $\sigma^2 = 0.035$ . (c) Spin-spin correlation  $\langle \mathbf{S}_i \cdot \mathbf{S}_j \rangle$  as a function of distance  $r_{ij} = |\mathbf{r}_j - \mathbf{r}_i|$  along the  $x$  direction at filling  $f = 0.485$ . Red dots show LLG results using NN models without Langevin noise, while blue lines correspond to ED–LLG simulations at  $T = 0.022$ .

a  $30 \times 30$  lattice. Fig. 4(a) compares NN-predicted exchange fields  $\mathbf{H}_i$  with exact results, while the deviation  $\delta = H_{\text{ML}} - H_{\text{exact}}$  follows a Gaussian distribution with variance  $\sigma^2 = 0.035$  [Fig. 4(b)]. The normal distribution of  $\delta$  suggests that the ML uncertainty may act as an effective temperature in Langevin dynamics. We then combined the trained NN with LLG dynamics to simulate a thermal quench from random spins at  $T = 0.022$  on a  $30 \times 30$  lattice, using identical parameters as in the ED reference. The resulting spin–spin correlations, shown in Fig. 4(c) for filling  $f = 0.485$  (1.5% hole doping), agree closely with ED–LLG results, confirming the accuracy and dynamical transferability of the ML force field.

Large-scale quench simulations were performed using the trained ML model on a  $100 \times 100$  lattice. Figure 5(a) shows snapshots of the local spin correlation, defined as the average over four nearest-neighbor bonds,  $b_i = (\mathbf{S}_i \cdot \mathbf{S}_{i+\mathbf{x}} + \mathbf{S}_i \cdot \mathbf{S}_{i-\mathbf{x}} + \mathbf{S}_i \cdot \mathbf{S}_{i+\mathbf{y}} + \mathbf{S}_i \cdot \mathbf{S}_{i-\mathbf{y}})/4$ . Positive (negative)  $b_i$  corresponds to ferromagnetic (FM) [antiferromagnetic (AFM)] regions. The ML–LLG simulations reveal relaxation into an inhomogeneous state comprising extended AFM domains interspersed with small FM clusters.

We next analyze the kinetics of FM-domain growth. A FM cluster is defined as a connected region where all nearest-neighbor bonds exceed  $b_{\text{th}} = 0.5$ . The time evolution of the characteristic length  $L$  is shown in Fig. 5(b). Because the number of doped holes is conserved, the coarsening of such conserved fields follows the

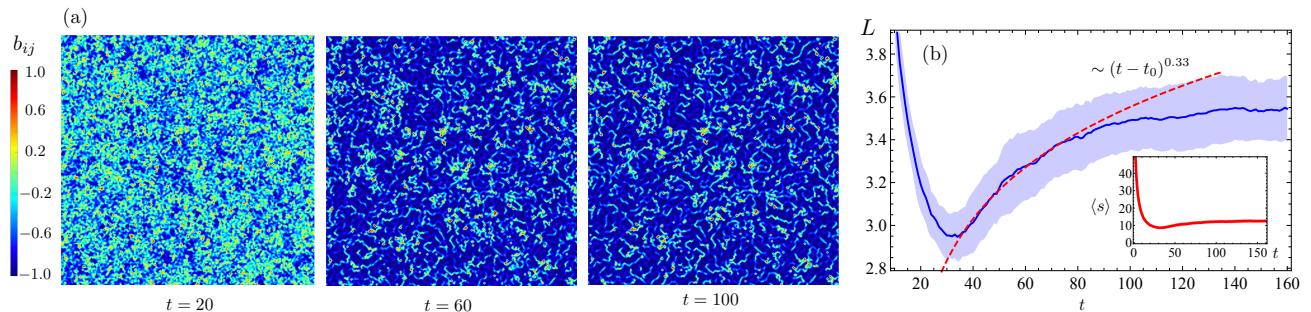


FIG. 5. (a) Density maps of local bond variables  $b(\mathbf{r}_i)$  at four different times during the ML–LLG simulation on a  $100 \times 100$  lattice with 1.5% hole doping. (b) Average linear size  $L = \langle s \rangle^{1/2}$  of FM clusters versus time after a thermal quench. The dash-dotted line denotes the  $t^{1/3}$  power-law growth, while the dashed line shows a sublogarithmic dependence  $L(t) \sim (\log t)^\beta$  with  $\beta = 0.11$ . The inset plots the time evolution of the average cluster size  $\langle s \rangle$ .

Cahn–Hilliard equation [84, 85] or LSW theory [77, 78], predicting  $L(t) \sim t^{1/3}$ . However, as shown in Fig. 5(b), this scaling holds only at early times; at later stages, the domain size  $L$  grows much more slowly than predicted by LSW theory.

The LSW theory describes diffusive interactions among minority-phase domains, where larger clusters grow by absorbing material from smaller ones via an evaporation–condensation mechanism. In our case, this corresponds to the migration of doped holes from small to large FM clusters. The early-stage  $t^{1/3}$  scaling likely reflects this process. As AFM correlations develop in the half-filled background, however, each doped hole becomes surrounded by parallel spins through the double-exchange mechanism, forming a self-trapped FM cloud. This localization suppresses hole evaporation and halts the coarsening process, leading to a breakdown of the LSW scenario.

## V. CONCLUSION AND OUTLOOK

In this paper, we have presented a scalable ML force-field framework for LLG simulations of itinerant electron magnets. Based on the principle of locality, the method expresses effective spin-dependent forces as functions of local spin environments using group-theoretical descriptors that rigorously preserve both lattice and spin symmetries. Analogous to the BP approach for ab initio MD simulations, the neural-network model predicts local exchange fields as energy gradients, achieving linear-scaling efficiency and high transferability across spin configurations. Applications to the prototypical s–d exchange model demonstrate the versatility of this framework and reveal nonequilibrium dynamical phenomena beyond the

reach of conventional methods.

While this study focuses on the BP-type formulation, other ML architectures provide complementary and often more flexible approaches. Convolutional neural networks (CNNs), with their intrinsic local connectivity, naturally implement the principle of locality and enable scalable ML force fields for spin systems [86, 87]. Recent advances further introduce elegant ways to embed both symmetry and scalability: equivariant neural networks enforce symmetry constraints directly within the architecture [88–90], while graph neural networks (GNNs) achieve linear scaling via localized message passing and symmetry-preserving transformations of equivalent graph elements [91–94]. Extending these advanced architectures to model spin dynamics in itinerant magnets represents a promising avenue for future work.

**Data availability** The data that support the findings of this study are openly available in [https://github.com/cherngroupUVA/ML\\_double\\_exchange](https://github.com/cherngroupUVA/ML_double_exchange) where one can find C and Python codes, trained model samples and data samples to successfully run the machine learning spin dynamics and reproduce results discussed in the main text.

## ACKNOWLEDGMENTS

This work was supported by the US Department of Energy Basic Energy Sciences under Contract No. DE-SC0020330. The authors acknowledge Research Computing at The University of Virginia for providing computational resources and technical support that have contributed to the results reported within this publication.

[1] A. N. Bogdanov and D. Yablonskii, Thermodynamically stable “vortices” in magnetically ordered crystals. the mixed state of magnets, *Zh. Eksp. Teor. Fiz* **95**, 178

(1989).

[2] U. K. Rößler, A. N. Bogdanov, and C. Pfleiderer, Spontaneous skyrmion ground states in magnetic metals, *Nature*

- 442**, 797 (2006).
- [3] S. Mühlbauer, B. Binz, F. Jonietz, C. Pfleiderer, A. Rosch, A. Neubauer, R. Georgii, and P. Böni, Skyrmion lattice in a chiral magnet, *Science* **323**, 915 (2009).
- [4] X. Z. Yu, Y. Onose, N. Kanazawa, J. H. Park, J. H. Han, Y. Matsui, N. Nagaosa, and Y. Tokura, Real-space observation of a two-dimensional skyrmion crystal, *Nature* **465**, 901 (2010).
- [5] X. Z. Yu, N. Kanazawa, Y. Onose, K. Kimoto, W. Z. Zhang, S. Ishiwata, Y. Matsui, and Y. Tokura, Near room-temperature formation of a skyrmion crystal in thin-films of the helimagnet fege, *Nature Materials* **10**, 106 (2011).
- [6] S. Seki, X. Z. Yu, S. Ishiwata, and Y. Tokura, Observation of skyrmions in a multiferroic material, *Science* **336**, 198 (2012).
- [7] N. Nagaosa and Y. Tokura, Topological properties and dynamics of magnetic skyrmions, *Nature Nanotechnology* **8**, 899 (2013).
- [8] E. Dagotto, *Nanoscale phase separation and colossal magnetoresistance* (Springer Verlag, Berlin, 2002).
- [9] E. Dagotto, Complexity in strongly correlated electronic systems, *Science* **309**, 257 (2005).
- [10] A. Moreo, S. Yunoki, and E. Dagotto, Phase separation scenario for manganese oxides and related materials, *Science* **283**, 2034 (1999).
- [11] E. Dagotto, T. Hotta, and A. Moreo, Colossal magnetoresistant materials: the key role of phase separation, *Physics Reports* **344**, 1 (2001).
- [12] N. Mathur and P. Littlewood, Mesoscopic texture in manganites, *Physics Today* **56**, 25 (2003).
- [13] E. L. Nagaev, *Colossal Magnetoresistance and Phase Separation in Magnetic Semiconductors* (Imperial College Press, London, 2002).
- [14] M. Fäth, S. Freisem, A. A. Menovsky, Y. Tomioka, J. Aarts, and J. A. Mydosh, Spatially inhomogeneous metal-insulator transition in doped manganites, *Science* **285**, 1540 (1999).
- [15] C. Renner, G. Aeppli, B.-G. Kim, Y.-A. Soh, and S.-W. Cheong, Atomic-scale images of charge ordering in a mixed-valence manganite, *Nature* **416**, 518 (2002).
- [16] M. B. Salamon and M. Jaime, The physics of manganites: Structure and transport, *Rev. Mod. Phys.* **73**, 583 (2001).
- [17] W. Kohn, Density functional and density matrix method scaling linearly with the number of atoms, *Phys. Rev. Lett.* **76**, 3168 (1996).
- [18] E. Prodan and W. Kohn, Nearsightedness of electronic matter, *Proceedings of the National Academy of Sciences* **102**, 11635 (2005).
- [19] J. Behler and M. Parrinello, Generalized neural-network representation of high-dimensional potential-energy surfaces, *Phys. Rev. Lett.* **98**, 146401 (2007).
- [20] A. P. Bartók, M. C. Payne, R. Kondor, and G. Csányi, Gaussian approximation potentials: The accuracy of quantum mechanics, without the electrons, *Phys. Rev. Lett.* **104**, 136403 (2010).
- [21] Z. Li, J. R. Kermode, and A. De Vita, Molecular dynamics with on-the-fly machine learning of quantum-mechanical forces, *Phys. Rev. Lett.* **114**, 096405 (2015).
- [22] A. V. Shapeev, Moment tensor potentials: A class of systematically improvable interatomic potentials, *Multiscale Modeling & Simulation* **14**, 1153 (2016).
- [23] J. Behler, Perspective: Machine learning potentials for atomistic simulations, *The Journal of Chemical Physics* **145**, 170901 (2016).
- [24] V. Botu, R. Batra, J. Chapman, and R. Ramprasad, Machine learning force fields: Construction, validation, and outlook, *The Journal of Physical Chemistry C* **121**, 511 (2017).
- [25] J. S. Smith, O. Isayev, and A. E. Roitberg, Ani-1: an extensible neural network potential with dft accuracy at force field computational cost, *Chem. Sci.* **8**, 3192 (2017).
- [26] L. Zhang, J. Han, H. Wang, R. Car, and W. E, Deep potential molecular dynamics: A scalable model with the accuracy of quantum mechanics, *Phys. Rev. Lett.* **120**, 143001 (2018).
- [27] V. L. Deringer, M. A. Caro, and G. Csanyi, Machine learning interatomic potentials as emerging tools for materials science, *Advanced Materials* **31**, 1902765 (2019).
- [28] R. T. McGibbon, A. G. Taube, A. G. Donchev, K. Siva, F. Hernandez, C. Hargus, K.-H. Law, J. L. Klepeis, and D. E. Shaw, Improving the accuracy of möller-pleiset perturbation theory with neural networks, *The Journal of Chemical Physics* **147**, 161725 (2017).
- [29] H. Suwa, J. S. Smith, N. Lubbers, C. D. Batista, G.-W. Chern, and K. Barros, Machine learning for molecular dynamics with strongly correlated electrons, *Phys. Rev. B* **99**, 161107 (2019).
- [30] S. Chmiela, A. Tkatchenko, H. E. Saucedo, I. Poltavsky, K. T. Schütt, and K.-R. Müller, Machine learning of accurate energy-conserving molecular force fields, *Science Advances* **3**, e1603015 (2017).
- [31] S. Chmiela, H. E. Saucedo, K.-R. Müller, and A. Tkatchenko, Towards exact molecular dynamics simulations with machine-learned force fields, *Nature Communications* **9**, 3887 (2018).
- [32] H. E. Saucedo, M. Gastegger, S. Chmiela, K.-R. Müller, and A. Tkatchenko, Molecular force fields with gradient-domain machine learning (GDML): Comparison and synergies with classical force fields, *The Journal of Chemical Physics* **153**, 124109 (2020).
- [33] O. T. Unke, S. Chmiela, H. E. Saucedo, M. Gastegger, I. Poltavsky, K. T. Schütt, A. Tkatchenko, and K.-R. Müller, Machine learning force fields, *Chemical Reviews* **121**, 10142 (2021).
- [34] P. Zhang, S. Zhang, and G.-W. Chern, Descriptors for machine learning model of generalized force field in condensed matter systems (2022), [arXiv:2201.00798 \[cond-mat.str-el\]](https://arxiv.org/abs/2201.00798).
- [35] S. Zhang, P. Zhang, and G.-W. Chern, Anomalous phase separation in a correlated electron system: Machine-learning enabled large-scale kinetic monte carlo simulations, *Proceedings of the National Academy of Sciences* **119**, e2119957119 (2022).
- [36] C. Cheng, S. Zhang, and G.-W. Chern, Machine learning for phase ordering dynamics of charge density waves, *Phys. Rev. B* **108**, 014301 (2023).
- [37] S. Ghosh, S. Zhang, C. Cheng, and G.-W. Chern, Kinetics of orbital ordering in cooperative jahn-teller models: Machine-learning enabled large-scale simulations, *Phys. Rev. Mater.* **8**, 123602 (2024).
- [38] P. Zhang, P. Saha, and G.-W. Chern, Machine learning dynamics of phase separation in correlated electron magnets (2020), [arXiv:2006.04205 \[cond-mat.str-el\]](https://arxiv.org/abs/2006.04205).
- [39] P. Zhang and G.-W. Chern, Arrested phase separation in double-exchange models: Large-scale simulation enabled by machine learning, *Phys. Rev. Lett.* **127**, 146401

- (2021).
- [40] P. Zhang and G.-W. Chern, Machine learning nonequilibrium electron forces for spin dynamics of itinerant magnets, *npj Computational Materials* **9**, 32 (2023).
- [41] M. Shi, S. Zhang, and G.-W. Chern, Machine learning force-field models for metallic spin glass (2023), [arXiv:2311.16964 \[cond-mat.dis-nn\]](https://arxiv.org/abs/2311.16964).
- [42] Y. Fan, S. Zhang, and G.-W. Chern, Coarsening of chiral domains in itinerant electron magnets: A machine learning force-field approach, *Phys. Rev. B* **110**, 245105 (2024).
- [43] D. Marx and J. Hutter, *Ab initio molecular dynamics: basic theory and advanced methods* (Cambridge University Press, 2009).
- [44] M. A. Ruderman and C. Kittel, Indirect Exchange Coupling of Nuclear Magnetic Moments by Conduction Electrons, *Phys. Rev.* **96**, 99 (1954).
- [45] T. Kasuya, A Theory of Metallic Ferro- and Antiferromagnetism on Zener's Model, *Prog. Theor. Phys.* **16**, 45 (1956).
- [46] K. Yosida, Magnetic properties of Cu-Mn alloys, *Phys. Rev.* **106**, 893 (1957).
- [47] A. Paszke, S. Gross, S. Chintala, G. Chanan, E. Yang, Z. DeVito, Z. Lin, A. Desmaison, L. Antiga, and A. Lerer, Automatic differentiation in pytorch, in *NIPS 2017 Workshop on Autodiff* (2017).
- [48] A. G. Baydin, B. A. Pearlmutter, A. A. Radul, and J. M. Siskind, Automatic differentiation in machine learning: a survey, *Journal of Machine Learning Research* **18**, 1 (2018).
- [49] J. Behler, Atom-centered symmetry functions for constructing high-dimensional neural network potentials, *The Journal of Chemical Physics* **134**, 074106 (2011).
- [50] L. M. Ghiringhelli, J. Vybiral, S. V. Levchenko, C. Draxl, and M. Scheffler, Big data of materials science: Critical role of the descriptor, *Phys. Rev. Lett.* **114**, 105503 (2015).
- [51] A. P. Bartók, R. Kondor, and G. Csányi, On representing chemical environments, *Phys. Rev. B* **87**, 184115 (2013).
- [52] R. Drautz, Atomic cluster expansion for accurate and transferable interatomic potentials, *Phys. Rev. B* **99**, 014104 (2019).
- [53] L. Himanen, M. O. Jäger, E. V. Morooka, F. Federici Canova, Y. S. Ranawat, D. Z. Gao, P. Rinke, and A. S. Foster, Dscribe: Library of descriptors for machine learning in materials science, *Computer Physics Communications* **247**, 106949 (2020).
- [54] H. Huo and M. Rupp, Unified representation of molecules and crystals for machine learning, *Machine Learning: Science and Technology* **3**, 045017 (2022).
- [55] J. Ma, P. Zhang, Y. Tan, A. W. Ghosh, and G.-W. Chern, Machine learning electron correlation in a disordered medium, *Phys. Rev. B* **99**, 085118 (2019).
- [56] Y.-H. Liu, S. Zhang, P. Zhang, T.-K. Lee, and G.-W. Chern, Machine learning predictions for local electronic properties of disordered correlated electron systems, *Phys. Rev. B* **106**, 035131 (2022).
- [57] R. Kondor, A novel set of rotationally and translationally invariant features for images based on the non-commutative bispectrum (2007), [arXiv:cs/0701127 \[cs.CV\]](https://arxiv.org/abs/cs/0701127).
- [58] I. Martin and C. D. Batista, Itinerant Electron-Driven Chiral Magnetic Ordering and Spontaneous Quantum Hall Effect in Triangular Lattice Models, *Phys. Rev. Lett.* **101**, 156402 (2008).
- [59] Y. Akagi and Y. Motome, Spin chirality ordering and anomalous hall effect in the ferromagnetic kondo lattice model on a triangular lattice, *Journal of the Physical Society of Japan* **79**, 083711 (2010).
- [60] Y. Kato, I. Martin, and C. D. Batista, Stability of the spontaneous quantum hall state in the triangular kondo-lattice model, *Phys. Rev. Lett.* **105**, 266405 (2010).
- [61] M. Azhar and M. Mostovoy, Incommensurate spiral order from double-exchange interactions, *Phys. Rev. Lett.* **118**, 027203 (2017).
- [62] G.-W. Chern and C. D. Batista, Spontaneous quantum hall effect via a thermally induced quadratic fermi point, *Phys. Rev. Lett.* **109**, 156801 (2012).
- [63] G.-W. Chern, Noncoplanar Magnetic Ordering Driven by Itinerant Electrons on the Pyrochlore Lattice, *Phys. Rev. Lett.* **105**, 226403 (2010).
- [64] A. Weiße, G. Wellein, A. Alvermann, and H. Fehske, The kernel polynomial method, *Rev. Mod. Phys.* **78**, 275 (2006).
- [65] K. Barros and Y. Kato, Efficient langevin simulation of coupled classical fields and fermions, *Phys. Rev. B* **88**, 235101 (2013).
- [66] Z. Wang, G.-W. Chern, C. D. Batista, and K. Barros, Gradient-based stochastic estimation of the density matrix, *The Journal of Chemical Physics* **148**, 094107 (2018).
- [67] A. Paszke, S. Gross, F. Massa, A. Lerer, J. Bradbury, G. Chanan, T. Killeen, Z. Lin, N. Gimelshein, L. Antiga, *et al.*, Pytorch: An imperative style, high-performance deep learning library, *Advances in neural information processing systems* **32** (2019).
- [68] V. Nair and G. E. Hinton, Rectified linear units improve restricted boltzmann machines, in *Proceedings of the 27th International Conference on International Conference on Machine Learning, ICML'10* (Omnipress, Madison, WI, USA, 2010) p. 807–814.
- [69] D. P. Kingma and J. Ba, Adam: A method for stochastic optimization (2014), [arXiv:1412.6980 \[cs.LG\]](https://arxiv.org/abs/1412.6980).
- [70] C. Zener, Interaction between the  $d$ -shells in the transition metals. ii. ferromagnetic compounds of manganese with perovskite structure, *Phys. Rev.* **82**, 403 (1951).
- [71] P. W. Anderson and H. Hasegawa, Considerations on double exchange, *Phys. Rev.* **100**, 675 (1955).
- [72] P. G. de Gennes, Effects of double exchange in magnetic crystals, *Phys. Rev.* **118**, 141 (1960).
- [73] Schulz, H.J., Domain walls in a doped antiferromagnet, *J. Phys. France* **50**, 2833 (1989).
- [74] V. J. Emery, S. A. Kivelson, and H. Q. Lin, Phase separation in the  $t$ - $j$  model, *Phys. Rev. Lett.* **64**, 475 (1990).
- [75] S. R. White and D. J. Scalapino, Phase separation and stripe formation in the two-dimensional  $t - j$  model: A comparison of numerical results, *Phys. Rev. B* **61**, 6320 (2000).
- [76] J. M. Tranquada, B. J. Sternlieb, J. D. Axe, Y. Nakamura, and S. Uchida, Evidence for stripe correlations of spins and holes in copper oxide superconductors, *Nature* **375**, 561 (1995).
- [77] I. Lifshitz and V. Slyozov, The kinetics of precipitation from supersaturated solid solutions, *Journal of Physics and Chemistry of Solids* **19**, 35 (1961).
- [78] C. Wagner, Theorie der alterung von niederschlagen durch umlosen, *Z. Elektrochem* **65**, 581 (1961).
- [79] C. M. Varma, Electronic and magnetic states in the  $g$ -

- ant magnetoresistive compounds, *Phys. Rev. B* **54**, 7328 (1996).
- [80] S. Yunoki, J. Hu, A. L. Malvezzi, A. Moreo, N. Furukawa, and E. Dagotto, Phase separation in electronic models for manganites, *Phys. Rev. Lett.* **80**, 845 (1998).
- [81] E. Dagotto, S. Yunoki, A. L. Malvezzi, A. Moreo, J. Hu, S. Capponi, D. Poilblanc, and N. Furukawa, Ferromagnetic kondo model for manganites: Phase diagram, charge segregation, and influence of quantum localized spins, *Phys. Rev. B* **58**, 6414 (1998).
- [82] A. Chattopadhyay, A. J. Millis, and S. Das Sarma,  $t = 0$  phase diagram of the double-exchange model, *Phys. Rev. B* **64**, 012416 (2001).
- [83] D. Pekker, S. Mukhopadhyay, N. Trivedi, and P. M. Goldbart, Double-exchange model for noninteracting electron spins coupled to a lattice of classical spins: Phase diagram at zero temperature, *Phys. Rev. B* **72**, 075118 (2005).
- [84] J. W. Cahn and J. E. Hilliard, Free energy of a nonuniform system. i. interfacial free energy, *The Journal of Chemical Physics* **28**, 258 (1958).
- [85] P. C. Hohenberg and B. I. Halperin, Theory of dynamic critical phenomena, *Rev. Mod. Phys.* **49**, 435 (1977).
- [86] X. Cheng, S. Zhang, P. C. H. Nguyen, S. Azarfar, G.-W. Chern, and S. S. Baek, Convolutional neural networks for large-scale dynamical modeling of itinerant magnets, *Phys. Rev. Res.* **5**, 033188 (2023).
- [87] A. Tyberg, Y. Fan, and G.-W. Chern, Machine learning force field model for kinetic monte carlo simulations of itinerant ising magnets, *Phys. Rev. B* **111**, 235132 (2025).
- [88] N. Thomas, T. Smidt, S. Kearnes, L. Yang, L. Li, K. Kohlhoff, and P. Riley, **Tensor field networks: Rotation- and translation-equivariant neural networks for 3d point clouds** (2018), [arXiv:1802.08219 \[cs.LG\]](https://arxiv.org/abs/1802.08219).
- [89] B. Anderson, T.-S. Hy, and R. Kondor, Cormorant: covariant molecular neural networks, in *Proceedings of the 33rd International Conference on Neural Information Processing Systems* (Curran Associates Inc., Red Hook, NY, USA, 2019).
- [90] R. J. L. Townshend, B. Townshend, S. Eismann, and R. O. Dror, **Geometric prediction: Moving beyond scalars** (2020), [arXiv:2006.14163 \[cs.LG\]](https://arxiv.org/abs/2006.14163).
- [91] F. Scarselli, M. Gori, A. C. Tsoi, M. Hagenbuchner, and G. Monfardini, The graph neural network model, *IEEE Transactions on Neural Networks* **20**, 61 (2009).
- [92] P. Reiser, M. Neubert, A. Eberhard, L. Torresi, C. Zhou, C. Shao, H. Metni, C. van Hoesel, H. Schopmans, T. Sommer, and P. Friederich, Graph neural networks for materials science and chemistry, *Communications Materials* **3**, 93 (2022).
- [93] S. Batzner, A. Musaelian, L. Sun, M. Geiger, J. P. Mailoa, M. Kornbluth, N. Molinari, T. E. Smidt, and B. Kozinsky, E(3)-equivariant graph neural networks for data-efficient and accurate interatomic potentials, *Nature Communications* **13**, 2453 (2022).
- [94] I. Batatia, S. Batzner, D. P. Kovács, A. Musaelian, G. N. C. Simm, R. Drautz, C. Ortner, B. Kozinsky, and G. Csányi, The design space of e(3)-equivariant atom-centred interatomic potentials, *Nature Machine Intelligence* **7**, 56 (2025).